ISR measurements and modeling of high-latitude solar photoionization

R. A. Doe

Center for Geospace Studies, SRI International, Menlo Park, California

J. P. Thayer

Department of Aerospace Engineering Sciences, University of Colorado, Boulder, Colorado

S. C. Solomon

High Altitude Observatory, National Center for Atmospheric Research, Boulder, Colorado

Abstract.

A nine-year database of sunlit *E*-region electron density altitude profiles (N_e(z)) measured by the Sondrestrom incoherent scatter radar (ISR) has been partitioned over a parameter space of 10.7 cm solar radio flux ($F_{10.7}$) and solar zenith angle (χ) to investigate long-term solar and thermospheric variability and to validate a contemporary EUV photoionization model. A two-stage filter, which rejects N_e(z) profiles with large Hall-to-Pedersen conductance ratio and incorporates an MLT-dependent correction factor for low-energy precipitation, is used to mitigate auroral contamination. Resultant filtered mean sunlit N_e(z) is compared with subauroral N_e measured for the same $F_{10.7}$ and χ conditions at the Millstone Hill ISR in order to confirm adequate high-energy auroral rejection. Mean N_e, as expected, increases with solar activity and decreases with large χ. Radar model comparison indicates that across all parameter space and for altitudes from 105 to 180 km, the GLOW model estimates are within 5% of the ISR mean with the contribution from photoelectrons accounting for 30 to 50% of equilibrium ion density. Above 180 km, the GLOW model slightly overestimates the height of the F1-layer. Radar model comparison also reveals a low altitude N_e enhancement for high solar activity at altitudes commensurate with 3 to 7 nm XUV and H Lyman-β radiances. The variance of the ISR mean N_e is shown to be greatest at low $F_{10.7}$ (solar minimum). Simulated N_e variance envelopes, given by perturbing the GLOW model neutral atmosphere input by the measured A_p, $F_{10.7}$, and T_e extrema, are narrower than ISR derived geophysical variance envelopes at solar minimum. We find no evidence for solar cycle control of low-energy precipitation and thus we attribute the observed N_e variance at solar minimum to variability in solar EUV flux. In order to address estimation of N_e at altitudes where GLOW model photochemical equilibrium assumptions are invalid, we provide an empirical model for Sondrestrom quiet time photoionization N_e(z) as a function of $F_{10.7}$ and χ.

1. Introduction

Plasma density of the daylit high-latitude ionosphere is produced primarily by structured and diffuse auroral precipitation as well as solar extreme ultraviolet (EUV) illumination. Prior incoherent scatter radar (ISR) studies of the quiet daylit ionosphere have considered the control of height-integrated conductivity during quiet summertime conditions as parameterized by 10.7 cm solar radio flux ($F_{10.7}$) and solar zenith angle (χ) [*Robinson and Vondrak*, 1984; *Rasmussen et al.* 1988; *Moen and Brekke*, 1993 and references therein]. Such quiet time conductance models provide important mean inputs to magnetohydrodynamic and assimilated models of high latitude electrodynamics, but ignore any information gleaned by the altitude distribution of the equilibrium mean electron density N_e(z) or variations around the mean.

Herein, we seek to directly study the nature of solar control over quiet time plasma density profiles by examining mean and variance N_e derived from a nine year ISR database as partitioned on a parameter space of $F_{10.7}$ and χ. We then compare ISR-derived mean and variance N_e with a contemporary EUV model, suitably perturbed to estimate long-term thermospheric variability, in order to address candidate sources for observed N_e variability. Our baseline model for comparison is the GLOW model [*Solomon et al.*, 1988; *Solomon and Abreu*, 1989; *Bailey et al.*, 2002; *Solomon and Qian*, 2003].

Comparison of ISR and GLOW modeled mean N_e serves to validate the efficacy of contemporary EUV spectral models, to investigate the relative importance of photoelectron

Paper number 2003JA011129.
0148-0227/05/2003JA011129$9.00

impact, and to highlight the solar cycle evolution of specific spectral features. Morphological features of ISR $N_e(z)$ at altitudes below 120, for example, are dominated by photoionization from soft X-ray ultraviolet (XUV), solar H Lyman-β, and CIII lines — and thus one can monitor solar cycle evolution of these spectral components by studying the associated evolution of lower *E*-region photo-produced $N_e(z)$ structure. Comparison of ISR and modeled N_e variance (δN_e) can likewise address the long-term variability in solar spectra over timescales much longer than the operational lifetime of satellite EUV sensors. Specifically, the ISR measurements described herein span the period identified as the "EUV hole" by *Tobiska et al.* [2000]. Finally, we create an ISR-based empirical model of quiet daytime N_e that reproduces ionospheric structure at altitudes where GLOW model photochemical equilibrium assumptions are not valid.

In the following sections, we describe analysis of nearly nine years of Sondrestrom ISR N_e data with a two-stage filtering scheme designed to remove high- and low-energy auroral ionization effects. Because our auroral filter is based on conductance ratios, we can directly compare the ensemble of Sondrestrom conductance measurements with the prior ISR-based quiet time models of *Rasmussen et al.* [1988] and *Moen and Brekke* [1993]. Of over 67,000 input $N_e(z)$ profiles, the 8541 that survived filtering are partitioned into bins of $F_{10.7}$ and χ, where $F_{10.7}$ is the average of daily and 81-day mean solar 10.7 cm radio flux. Filtered $N_e(z)$ is then compared with subauroral $N_e(z)$ measured at the Millstone Hill ISR to confirm adequate high-energy auroral rejection.

In a manner similar to the comparison of individual subauroral $N_e(z)$ profiles with EUV aeronomical models [*Buonsanto et al.*, 1995], our study evaluates how well a contemporary EUV model reproduces ISR mean $N_e(z)$ (Section 4). This model uses a 1 nm implementation of the solar spectra from the EUV model for aeronomical calculations (EUVAC) [*Richards et al.*, 1994], additional short XUV spectral components, and the GLOW photoelectron and photochemical model [*Solomon et al.*, 1988; *Solomon and Abreu*, 1989; *Bailey et al.*, 2002; *Solomon and Qian*, 2003]. Across all bins of $F_{10.7} - \chi$ parameter space, the GLOW model is shown to accurately predict ISR-derived mean N_e.

In Section 5 we highlight features in the ten best sampled ISR $N_e(z)$ bins to address long-term geophysical behavior of mean and variance N_e. Specifically, we note a general broadening of variance $N_e(z)$ at solar minimum, and the emergence of a low-altitude (107 to 112 km) N_e enhancement at solar maximum. Thermospheric perturbations to the GLOW model are used to argue that the observed variance in ISR measured N_e at solar minimum is driven by variations in the solar spectra. Finally, we present an ISR-based empirical model for $N_e(z)$ below 200 km as described by F1-layer peak density (NmF1), altitude at peak density (HmF1), and layer width across the $F_{10.7} - \chi$ parameter space.

2. Description of ISR Data

The database assembled herein comprises 67,603 $N_e(z)$ profiles measured along the local magnetic field line over a period from 11 April 1994 to 9 January 2003. This period spans the minimum between solar cycle peaks 22 and 23 as well as the maximum of solar cycle 23. A significant portion of these $N_e(z)$ profiles were acquired during monthly multi-day "World Day" runs and thus samples are well distributed — especially over summer months when χ reaches its seasonal minimum.

From April 1994 onward, the Sondrestrom ISR has probed the auroral ionosphere with a dual pulse mode that simultaneously measures plasma parameters in the *E* region and *F* region [*Kelly et al.*, 1995]. The *E*-region mode employs the 16-baud alternating code scheme described by *Lehtinen and Häggström* [1987] and provides 3 km range resolution with no range ambiguities. The *F*-region mode, on the other hand, consists of a single 320 μs uncoded "long pulse" (LP) with 48 km range resolution. Our data have been assembled from merged A16/LP profiles that are composites of the high resolution "alternating code" (A16) and lower resolution LP data streams.

The high-resolution A16 scheme was implemented in part so that conductivity calculations would not suffer from low-resolution LP sampling in an altitude regime wherein Hall and Pedersen mobility terms are sharply peaked. We consider briefly the nature of these mobility terms.

Calculation of conductivity proceeds directly from a calculation of Pedersen and Hall mobilities as described by *Rishbeth and Garriott* [1969]. The calculation of mobility per unit charge (ratio of mean scattering time to mass) accounts for scattering contributions from both random thermal motions and ordered gyrorotation of ions and electrons in a background neutral atmosphere. Canonical forms for Pedersen mobility (k_P) and Hall mobility (k_H) are given:

$$k_P = \frac{\nu/m}{\left(\nu^2 + \Omega^2\right)} \tag{1}$$

$$k_H = \frac{\Omega/m}{\left(\nu^2 + \Omega^2\right)} \tag{2}$$

where ν is momentum transfer collision frequency of the ion or electron with background neutrals, m is mass of the ion or electron, and Ω is the ion or electron gyrofrequency (qB/m), where q is the ion or electron charge. Pedersen and Hall conductivity can now be given:

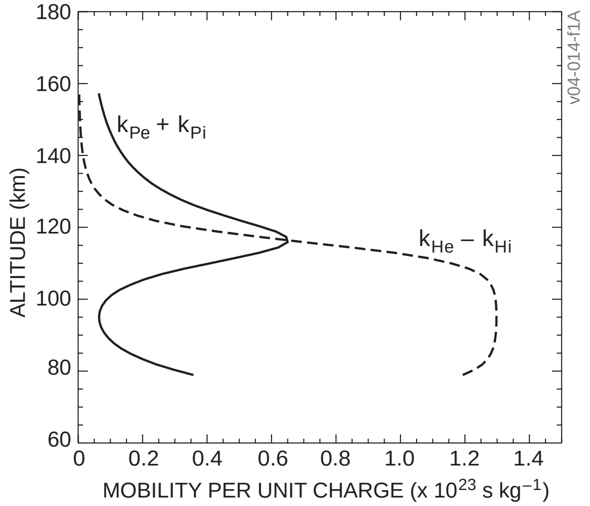

Figure 1. Pedersen and Hall Mobility Arguments

$$\sigma_P = \mathrm{N}_e q^2 \left(k_{P_e} + k_{P_i} \right) \tag{3}$$

$$\sigma_H = \mathrm{N}_e q^2 \left(k_{H_e} - k_{H_i} \right). \tag{4}$$

Figure 1 shows the altitude behavior of the Pedersen and Hall mobility terms in equations (3) and (4). If ionospheric densities were only probed with the 48 km long pulse, then the precision of calculated Pedersen and Hall conductivities would be greatly degraded. This point is relevant to the current study as we intend to use a conductance-based first-stage filter to remove N_e profiles dominated by high-energy auroral precipitation. The 3 km resolution of the A16 mode also ensures accurate sampling of *E*-region structure at altitudes sensitive to photoionization from select XUV and EUV spectral components.

Because A16 coding measures incoherent scatter from a 3 km range sample, its signal-to-noise ratio (SNR) is lower and usable altitude range is more restricted, when compared with the 48 km LP sample. All A16 and LP measurements used in this study were integrated for 60 s — sufficiently long to ensure usable A16 mode SNR in the *E* region.

A16/LP profile merging uses N_e error ($\delta\mathrm{N}_e$), provided by the ISR fitting program, to drive an altitude-dependent weighting that transitions smoothly from mostly A16 data at 90 km to mostly LP data at 200 km:

$$\mathrm{N}_e = \frac{(\delta\mathrm{N}_e^L)^2 \mathrm{N}_e^A + f\left(\delta\mathrm{N}_e^A\right)^2 \mathrm{N}_e^L}{(\delta\mathrm{N}_e^L)^2 + f\left(\delta N_e^A\right)^2}, \tag{5}$$

where the superscripts *L* and *A* denote LP and A16 measurements, respectively, and *f* is an exponential weighting factor:

$$f = a e^{(z-z_0)/H_0}. \tag{6}$$

Coefficients a, z_0, and scale height H_0 have been selected so that $(\delta\mathrm{N}_e^A)^2$ and $(\delta\mathrm{N}_e^L)^2$ have equal weighting at 170 km and so that LP contributions are attenuated a factor of 400 at 90 km (relative to 200 km). The variance in merged electron density is given by substituting $(\delta\mathrm{N}_e^A)^2$ and $(\delta\mathrm{N}_e^L)^2$ for N_e^A and N_e^L in equation (1).

Figure 2 provides examples of merged N_e profiles for active auroral and quiet daylit ($\chi = 74°$) conditions. The auroral profile shows how the coarse 48 km LP sampling attenuates the true peak of arc-related ionization at 115 km and adds an artifact below 103 km. The daytime profile, with a shape characteristic of an *E*-region ionosphere dominated by solar photoionization, shows less distortion from LP smearing. Hall-to-Pedersen conductance values have been calculated for all $\mathrm{N}_e(\mathrm{z})$ profiles and indicate that LP data overestimates Σ_H/Σ_P by approximately 11% relative to the merged values. We are now set to filter our ISR $\mathrm{N}_e(\mathrm{z})$ data ensemble for high-fidelity, quiet time, and sunlit conditions.

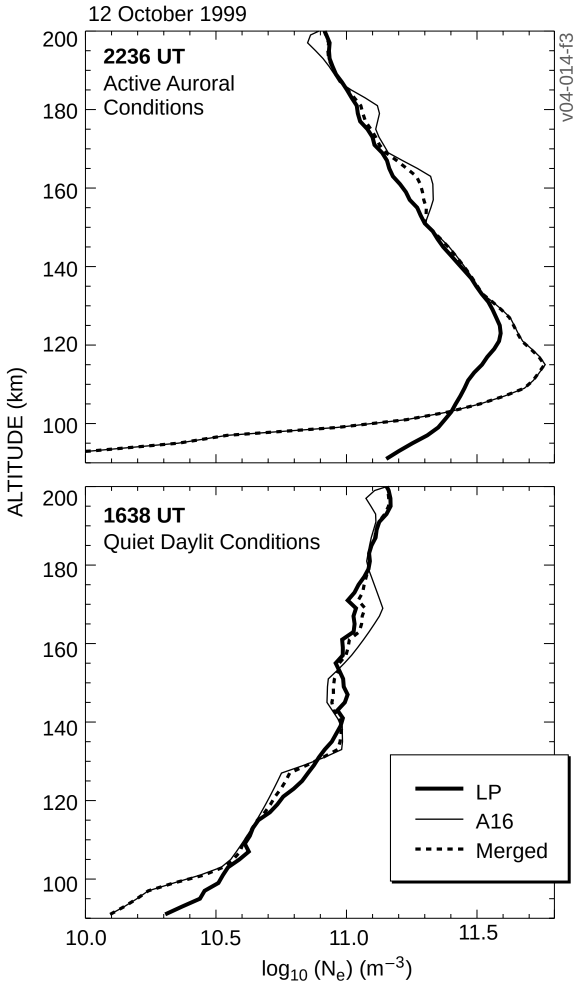

Figure 2. $N_e(z)$ for Auroral and Quiet Sunlit Conditions

3. Data Filtering and Partitioning

As a first-stage quality check, we seek to minimize inclusion of low SNR $\mathrm{N}_e(z)$ profiles and profiles with significant contributions from coarsely sampled LP measurements. Because we merge low SNR 3 km resolved A16 data with high SNR 48 km resolved LP data, these goals are mutually exclusive. We have optimized these two goals by rejecting profiles with average relative uncertainty greater than 28% in the *E* region. This ad hoc threshold is a compromise between our desire for high precision N_e and for avoidance of pulse smearing effects. N_e profiles with less than 28% N_e uncertainty are comprised of no less than 90% of available high resolution A16 samples at *E*-region altitudes. This relatively high proportion of A16 data inclusion drops precipitously as one imposes a smaller threshold in acceptable N_e uncertainty. This quality check rejects one third of the total number of profiles in our database to yield 44,000 for subsequent analysis. At this point we seek to remove profiles with significant auroral contamination.

Prior quiet time solar photoionization studies have typically selected only a handful of experiments for detailed analysis. Criteria for discrimination of nonauroral profiles have included minimal (local) magnetometer fluctuations [*Vickrey et al.*, 1982], large density excursions from mean N_e [*Robinson and Vondrak*, 1984], low k_P index [*Schlegel* 1988], and low A_P index along with ad hoc requirements for smoothness of diurnal conductance plots [*Brekke and Hall*, 1988; *Moen and Brekke*, 1993]. Filtering that depends on geomagnetic indices and human intervention are judged ineffective for our large database. A computationally efficient filtering method that differentiates sharply peaked auroral $N_e(z)$ from broadly peaked photoionization $N_e(z)$ is therefore an immediate goal.

3.1. First-Stage Conductance Ratio Filtering

Our approach will be to take advantage of the distinction in Hall and Pedersen conductivity profile shapes for auroral and solar forcing. If one assumes uniform $N_e(z)$ with altitude, then Pedersen conductivity peaks sharply around 120 km where the sum of electron and ion Pedersen mobilities maximize (see Figure 1). Hall conductivity, on the other hand, maintains a broad peak from 105 to 85 km, where the difference in electron and ion Hall mobility remains fairly constant. This altitude difference in conductance peak is further amplified for typical auroral $N_e(z)$ which, according to the shape of the electron energy spectrum, can sharply maximize above or below the Pedersen and Hall mobility peak altitudes.

More generally, it is noted that other shape-seeking filtering approaches could work just as well. For example, energy flux inversion techniques [*Semeter and Kamalabadi*, 2005] can be fine-tuned to seek out the broadly peaked $N_e(z)$ typical of solar forcing. A simple ad hoc kernel (i.e. sharply peaked Gaussian) can also be used in place of the mobility kernels of Figure 1, or a dedicated peak detection algorithm could be employed. All such methods, as well as our conductivity approach, break down for soft auroral $N_e(z)$ profiles that mimic the broad shape of photoionization profiles. We prefer to use a conductance based filter herein as it has a physics based connection to plasma – neutral collisions and is amenable to comparison with the results from prior ISR quiet time conductance models.

The behavior of energy-dependent height-integrated conductivity is commonly exploited to derive a proxy for characteristic energy of purely auroral precipitation. *Brekke et al.* [1974] suggested that the ratio of height-integrated Hall conductivity to height-integrated Pedersen conductivity would scale as electron energy, and *Robinson et al.* [1987] provide a prescription for calculating characteristic energy for assumed Maxwellian precipitation as a function of Σ_H/Σ_P.

Figure 3 exploits the fundamental difference in $N_e(z)$ profile shape by comparing solar EUV produced ionization with that from precipitating electrons. In this figure, solar photoionization $N_e(z)$ has been modeled for four combinations of $F_{10.7}$ and χ using the GLOW model as described in Section 4. $N_e(z)$ profiles corresponding to auroral impact have been modeled for Maxwellian electron spectra with a total number flux of 1×10^8 cm^2 s^{-1} for five values of characteristic energy (E_0) using the ionization expression of *Rees* [1989], the energy deposition distribution function for a unidirectional beam given by *Barrett and Hays* [1976], and the effective recombination coefficient given by *Vickrey et al.* [1982]:

$$\alpha = 2.5 \times 10^{-6} exp(-z/51.2) \qquad (7)$$

where z is in kilometers and α has units of cm^3 s^{-1}.

Hall and Pedersen conductivity was calculated for all profiles in Figure 3 using equations 1 through 4, the International Geomagnetic Reference Field [*IAGA*, 1985] for a calculation of ion and electron gyrofrequency (qB/m), and the ion and electron collision frequencies described in *Doe et al.* [1995]. Resultant conductivity profiles are then height integrated to yield conductance. The Hall to Pedersen conductance ratio is indicated by the color-coded key. These calculations suggest a measurable Σ_H/Σ_P distinction between photoionization and auroral impact ionization profiles, especially for the hardest electrons. This model calculation also suggests little change in the photoionization conductance ratio over a wide range of $F_{10.7}$ and χ values. This observation confirms the prior result from *Brekke and Hall*

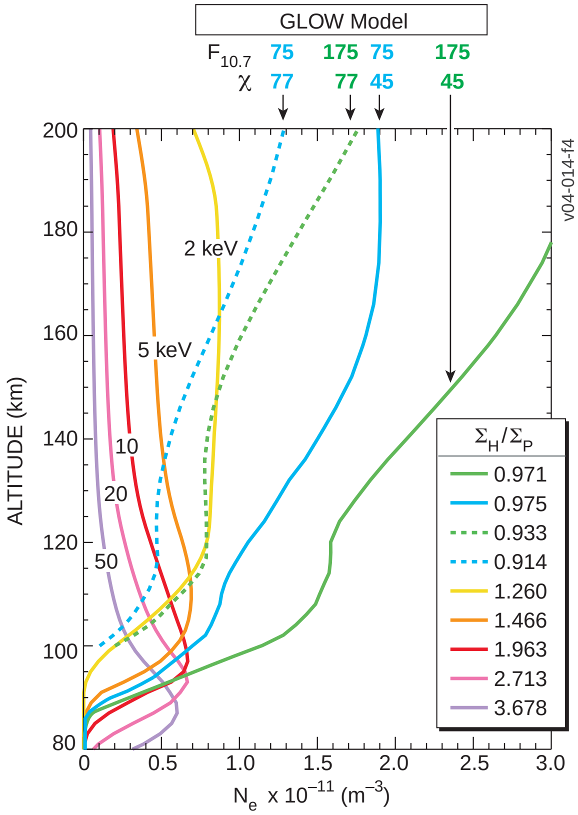

Figure 3. $N_e(z)$ for GLOW Model and Maxwellians

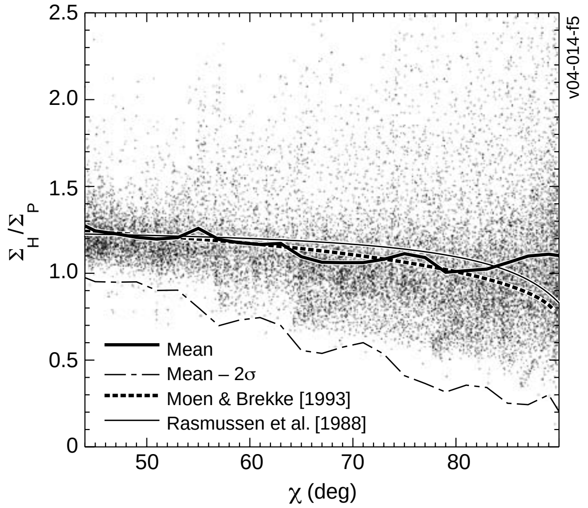

Figure 4. Σ_H/Σ_P for ISR Measurements and Models

[1988] that daytime Σ_H/Σ_P for quiet conditions is on the order of unity.

It is clear from Figure 3 that at some low energy, < 3 keV for this specific model, auroral impact ionization will be masked by solar effects. Let us now consider how impact and solar ionization are mixed in the context of an ion continuity expression appropriate to the *E*-region ionosphere (altitude < 200 km):

$$\frac{\partial N_e}{\partial t} = (q_e + q_{sol}) - \alpha (N_e)^2, \qquad (8)$$

where q_e is ion production from impact of energetic auroral electrons and q_{sol} is solar EUV photoionization and associated photoelectron impact. At these collisional altitudes, transport and diffusion terms have been neglected. α in this equation represents a composite for the electron recombination rate coefficient with the predominant *E*-region ions: O_2^+ and NO^+.

We now make a steady state assumption that *E*-region ion production equals recombination ion loss, an assumption that breaks down for rapid (< 1 s) fluctuations in the energy spectra of auroral electrons [*Semeter and Doe*, 2002], but is appropriate for timescales associated with gradual changes in solar forcing. Equilibrium $\mathrm{N}_e(\mathrm{z})$ now takes the form

$$\mathrm{N}_e(\mathrm{z}) = \sqrt{\frac{q_e + q_{sol}}{\alpha}}. \qquad (9)$$

It is clear that solar photon and impact ionization are intimately mixed in a way that can preclude reliable auroral isolation, especially for low-energy precipitation. We choose, therefore, a two-step approach to filtering out auroral contamination. Step one is to examine the ensemble of Σ_H/Σ_P for all daylit profiles in our database to determine a maximum threshold over which individual N_e profiles are likely contaminated with high-energy aurora. Step two applies this threshold to nighttime N_e profiles in order to derive a model for low-energy auroral precipitation (Section 3.2). This residual N_e is then used as a secondary correction to mean N_e in all bins of $\mathrm{F}_{10.7} - \chi$ parameter space.

Figure 4 summarizes Σ_H/Σ_P for all daylit profiles. This plot is overlain with Σ_H/Σ_P suggested by the photoequilibrium model of *Rasmussen et al.* [1988] and the low-order empirical model of *Moen and Brekke* [1993]. Mean and twice the standard deviation for Sondrestrom Σ_H/Σ_P has been calculated for 5-degree χ bins and overlain as solid and dashed lines, respectively. Note that from 41 to 81 degrees χ, both modeled ratios agree well with the mean ratio. We interpret this as an indication that the daylit mean Σ_H/Σ_P is dominated by solar photoionization effects. We also note that the 60 s profile integration time may have played a role in attenuating Σ_H/Σ_P spikes due to dynamic high-energy auroral arcs.

In this plot, excursions below the mean are likely due to the seasonal effect described by *Brekke and Hall* [1988] or by attenuation of soft X-rays and spectral lines with greatest impact below 120 (102.6 nm H Lyman-β and 97.7 nm CIII). Excursions above the mean are most likely due to auroral precipitation. We herein define the first step in auroral filtering by accepting all profiles bracketed by the Σ_H/Σ_P mean and mean minus twice the standard deviation and by $41^\circ < \chi < 81^\circ$. Such thresholding preserves the low Σ_H/Σ_P value predicted for the GLOW model (~0.9), and guarantees rejection of auroral arcs with greater than about 3 keV E_0. The 8541 profiles that survived filtering are now placed in bins of $\mathrm{F}_{10.7}$ and χ as shown in Figure 5. The bin occupancy shown in Figure 5 indicates heavy weighting for $\mathrm{F}_{10.7} < 85$ and $\mathrm{F}_{10.7} > 145$ — a reflection of the more frequent occurrence of $\mathrm{F}_{10.7}$ values at the solar minimum and maximum inflection points.

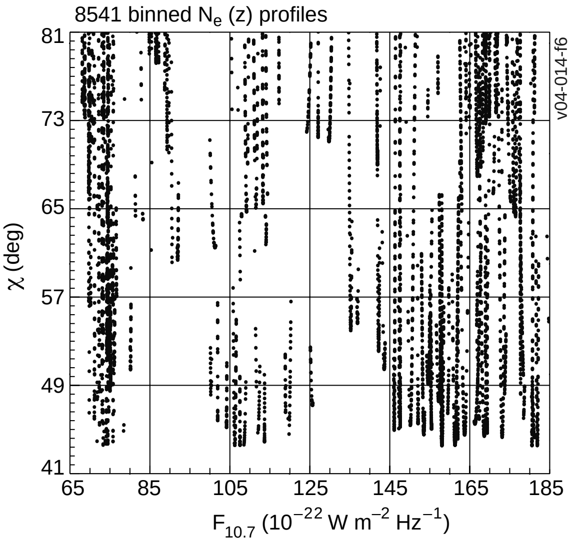

Figure 5. Data Partitioning

In each bin of Figure 5, and for each altitude 103 km < z < 200 km, mean N_e and variance N_e, $\mathrm{var}(\mathrm{N}_e)_{calc}$, are calculated. This observed variance has contributions from statistical uncertainty in the measurement, $\delta\mathrm{N}_e$, and the geophysical variability $\mathrm{var}(\mathrm{N}_e)$. Clearly, the geophysical variability will always be smaller than the total variance:

$$\mathrm{var}(\mathrm{N}_e) = \mathrm{var}(\mathrm{N}_e)_{calc} - (\overline{\delta\mathrm{N}_e})^2, \qquad (10)$$

where $\overline{\delta\mathrm{N}_e}$ represents the average ISR measurement error in N_e in a given bin at a given altitude. Standard deviation of N_e for each bin in Figure 5 is then given by $\sqrt{\mathrm{var}(\mathrm{N}_e)}$ and represents the geophysical fluctuations in N_e.

3.2. Removal of Low-Energy Ionization Sources

The N_e profiles selected by our Σ_H/Σ_P threshold filtering scheme also contains contributions from low energy electron precipitation (E_0 < 3 keV) and proton precipitation (E_0 < 13 keV) [*Galand and Richmond*, 2001] which must be removed in order to address solar forcing exclusively. This low-energy precipitation has the same range of energies as the non-discrete "continuous" aurora described by *Robinson and Vondrak* [1985] and *Whalen* [1983] — precipitation with a broad latitudinal distribution around a peak in the central latitude of the auroral oval. *Newell et al.* [1991] describe this unstructured precipitation as central plasma sheet or "diffuse" aurora, albeit with a higher maximum characteristic energy.

Without access to contemporaneous satellite spectrometer or imaging diagnostics, we seek a scheme that allows modeling of this low-energy precipitation as based on a statistical analysis of our entire nine-year data ensemble. The guiding assumption is that ionization due to low-energy precipitation contributes to equilibrium N_e in a similar manner for both sunlit and dark conditions. This assumption is supported by the *Newell et al.* [1996] analysis, which shows that non-discrete low-intensity auroral precipitation occurs with similar probability in all local sectors.

In the absence of solar EUV and hard auroral forcing, our filtered nightside ionospheric measurements are thus controlled solely by low-energy precipitation. At Sondrestrom's fixed geomagnetic latitude of 74°, we expect low-energy precipitation to be mainly controlled by proximity to the auroral oval. One might also expect geomagnetic activity or solar cycle control of low-energy precipitation. Thus, we choose to examine mean nightside N_e as parameterized by Magnetic Local Time (MLT), A_P index, and $F_{10.7}$ index. Specifically, we apply the daytime Σ_H/Σ_P selection threshold to 9132 nighttime $N_e(z)$ profiles in our database, bin the results by the desired parameter, and then extract mean N_e. Figure 6 summarizes resultant mean N_e as binned by MLT, A_P, and $F_{10.7}$.

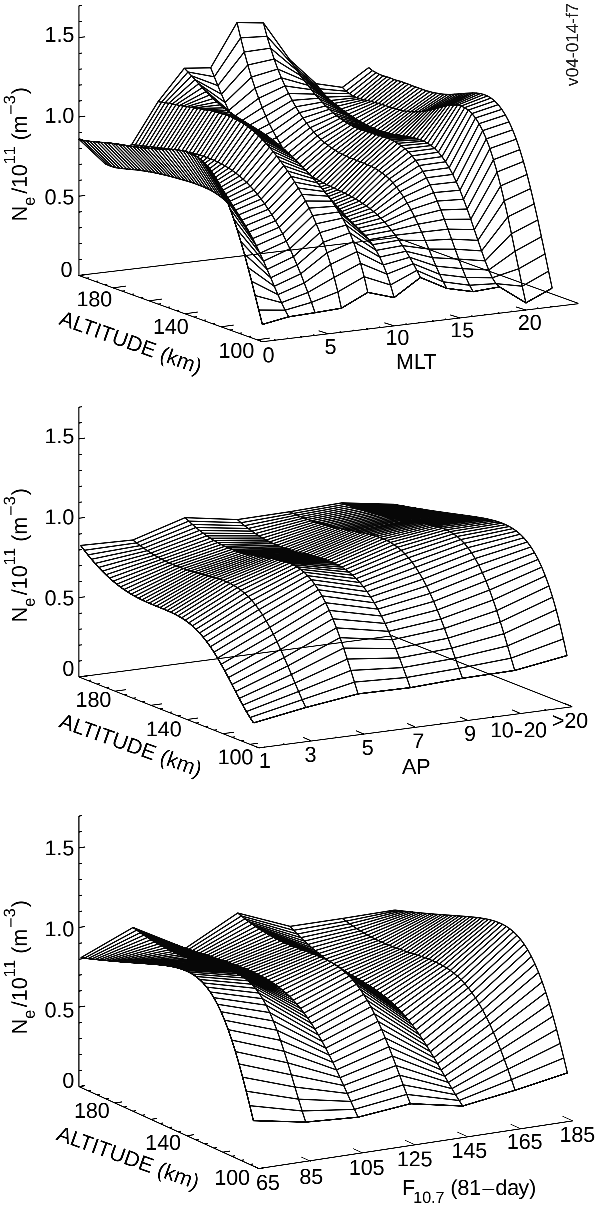

Figure 6. Low Energy N_e Parameterized by MLT, A_P, and $F_{10.7}$

This figure indicates that low-energy precipitation has its greatest dependence on MLT, with a significant peak at noon. This observation confirms that the Sondrestrom ISR has a high probability of measuring low-energy auroral precipitation in the cusp sector [*Doe et al.*, 2001]. To account for the MLT dependence of low-energy precipitation shown in Figure 6, we herein design a simple model.

To construct our model of low energy precipitation, we will consider the $N_e(z)$ profiles in the top panel of Figure 6 to be a basis set organized by MLT. This basis set is then transformed into a composite $N_e(z)$ profile by an MLT weighting scheme that is formed by examination of the range of MLT values within each bin of $F_{10.7} - \chi$ parameter space. Specifically, MLT weighting (W_{MLT}) is determined in each $F_{10.7} - \chi$ bin by calculating a histogram of MLT values as normalized by the total number of profile samples. Thus, for each bin, MLT-weighted ionization rate can be modeled:

$$q_{MLT} = \alpha(N_{MLT} W_{MLT})^2 \tag{11}$$

where N_{MLT} represents the $N_e(z)$ basis set in the top panel of Figure 6.

Substituting this q_{MLT} for q_e in equation (9), we can now solve for the "corrected" steady sate plasma density due to solar EUV in the absence of low- and high-energy precipitation (N_e^c):

$$N_e^c = \left[N_e^{\,2} - (N_{MLT} W_{MLT})^2\right]^{1/2} \tag{12}$$

where N_e is the mean density selected by our first stage Σ_H/Σ_P threshold filter. N_e^c is shown across all $F_{10.7} - \chi$ bins in Figure 7. In this figure, the 1 σ standard deviation envelope, calculated from equation (10), is shown in gray. In each bin, the total number of profiles contributing to mean and standard deviation is shown in the lower right hand corner.

3.3. Data Partitioning: Initial Observations

Mean N_e^c shown in Figure 7 displays the expected trend of increasing with solar activity, $F_{10.7}$, and decreasing with higher solar zenith angle χ. The deviation envelopes for 5 out of 7 bins with less than 70 samples are extremely narrow and are judged to be poor estimates for intrinsic N_e variability. When considering the ten best sampled bins (highlighted), we have greater confidence that the deviation envelope reflects actual geophysical variability and not statistical fluctuations. For 90% of these highly sampled bins, the deviation envelope is significantly wider at solar minimum ($F_{10.7} < 85$) than for solar maximum ($F_{10.7} > 145$) — a suggestion that solar EUV flux may have its greatest variance at solar minimum. We also note that a persistent low-altitude N_e enhancement is present in five out of six highly sampled bins for solar maximum conditions (shown with an arrow). This low altitude N_e bump emerges from an average of hundreds of profiles and is unlikely to be a spurious feature. We now consider comparison of ISR mean $N_e(z)$ with the GLOW model.

4. Comparison with the GLOW model

The GLOW model provides a reference EUV solar flux model ϕ_{UV}, additional amendments for XUV spectral components, an MSIS model [*Hedin*, 1987] based calculation of

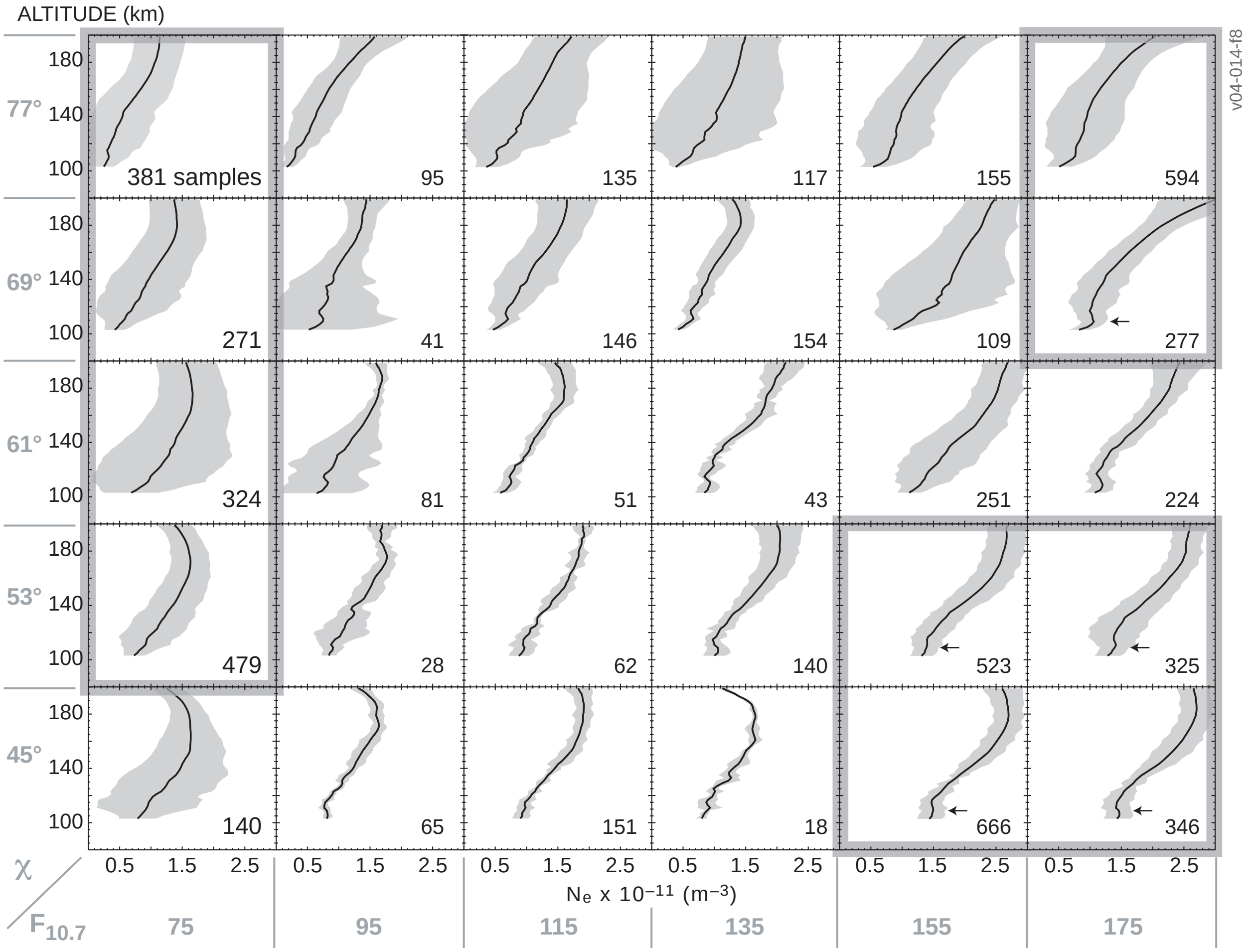

Figure 7. ISR Mean and Variance N$_e$ Across F$_{10.7}$ – χ Parameter Space. Low altitude N$_e$ enhancement at solar maximum is shown with arrows.

UV slant path loss and zenithal photoionization rate for multiple ion species, a calculation of photoelectron flux, and an *E*-region ion chemical code required to evaluate steady state N$_e$ from species specific ion production rate. For a given solar zenith angle χ, the zenithal ionization rate due to incident solar flux can be expressed as

$$q(z) = \sum_j \left[\beta_j(\lambda) \cdot \phi_{UV}(\lambda) \times e^{-\tau(\lambda,z,\chi)} \right] \cdot n_j(z) \quad (13)$$

where $q(z)$ has units of ion-electron pairs m^{-3} s^{-1}. In this equation, index j sums the contribution from major neutral species available for ionization (N, O, N$_2$, O$_2$). Unitless optical depth is given for χ less than 90° by *Rees* [1989]:

$$\tau = \sum_k \left[\sigma_k(\lambda) \int_z^{\infty} n_k(h) \left[1 - \left(\frac{R_e + z}{R_e + h} \right)^2 \sin^2 \chi \right]^{-1/2} dh \right], \quad (14)$$

where R_e is Earth radius, σ_k is photoabsorption cross section for the kth species, and k sums over major species subject to EUV photoabsorption (O, N$_2$, O$_2$). Implied in the above expressions for $q(z)$ and τ is a dependence on neutral composition, and thus we expect a functional dependence on the MSIS model input parameters, F$_{10.7}$ and A$_P$.

More specifically, we note that equation (13) describes mean ionization rate. Since one of our goals is to investigate photoionization variability, we should also consider intrinsic (δ) and modeled (Δ) variability:

$$q = \sum_j \left[\beta_j \cdot [\phi_{EUV} + \delta\phi_{EUV}] \times e^{-(\tau + \Delta\tau)} \right] \cdot (n_j + \Delta n_j), \quad (15)$$

where $\delta\phi_{EUV}$ is the long-term intrinsic variability of solar EUV flux, and $\Delta\tau$ and Δn_j are modeled variance envelopes that result from perturbing neutral composition and abundance. We have assumed that photoabsorption and photoionization cross sections are well known and do not contribute to ionization rate variability. For each bin in our F$_{10.7}$ – χ parameter space, we have determined the extrema in A$_P$ index and F$_{10.7}$ (± 10 units around bin center F$_{10.7}$) that can define an envelope of thermospheric variability through the MSIS model. In order to estimate worst-case thermospheric variability, we have run the MSIS model for each bin and have selected MSIS model output corresponding to the maximum excursion in T$_\infty$ across all parameter space. Thus, for our nearly nine-year data span, the envelope for perturbing the MSIS model within the GLOW model is effectively described by varying T_∞ from 850° K to 1630° K.

Since we wish to compare measured and modeled equilibrium N_e, and not q, we recognize an additional component of variability due to *E*-region photochemistry. In the GLOW model, which calculates composition and reactive dynamics of multiple ion species in a background MSIS neutral atmosphere, variability can be estimated by imposing the ISR $T_e(z)$ extrema on the simulation. This is due to the strong T_e dependence of charge exchange and molecular recombination rates. For example, if the ISR-derived maximum T_e is applied to the expressions for O_2^+ recombination coefficient given by *Walls and Dunn* [1974], then one calculates a minimum α. Conversely, if the ISR-derived minimum T_e is applied to the expression for NO^+ recombination coefficient given by *Torr and Torr* [1979], then one calculates maximum α. Using a perturbation approach, one can show the functional dependence of equilibrium N_e on perturbed α:

$$N_e = \sqrt{\frac{q}{\alpha + \Delta\alpha}}, \tag{16}$$

where α is the composite recombination rate of equation (7) and $\Delta\alpha$ is the difference between T_e perturbed maximum and minimum α. Since GLOW calculates recombination rates internally, a series of runs across all T_e and T_∞ extrema is used to establish an $N_e(z)$ variance envelope.

With relatively infrequent measurements of the solar EUV spectrum, ϕ_{UV} is commonly modeled with a reference spectrum appropriately scaled to estimate instantaneous UV radiance. *Hinteregger et al.* [1981] established an early spectral model based on Atmospheric Explorer E (AE-E) satellite and sounding rocket measurements that used $F_{10.7}$ as a proxy for solar EUV flux. In the intervening years, significant attention has been focused on correctly accounting for long- and short-term variability of $\phi_{UV}(\lambda)$ shortward of 25 nm — wavelengths responsible for significant ionization in the *E*-region ionosphere at altitudes below 160 km. Contemporary spectral solar models, such as EUVAC [*Richards et al.*, 1994] and SOLAR2000 [*Tobiska et al.*, 2000] have preferentially increased the mean flux of the *Hinteregger et al.* [1981] spectrum in these short λ bins to reconcile model calculations with photoelectron flux measurements during the AE-E satellite epoch. Recent measurements of solar soft X-ray fluxes by SNOE (Student Nitric Oxide Experiment) [*Solomon et al.*, 2001] and from the TIMED (Thermosphere – Ionosphere – Mesosphere and Dynamics Explorer) satellite [*Woods et al.*, 2005] have generally confirmed the short wavelength performance of EUVAC model scaling.

The EUVAC solar flux model specifies ϕ_{UV} for twenty 5 nm wide bins from 5 to 105 nm, corresponding to the solar EUV continuum, and 17 additional bins corresponding to discrete line emission from multiply ionized species. Refined low-altitude performance is achieved in GLOW by using a 1 nm version of the EUVAC solar flux and appending the short wavelength portion of the EUVAC reference spectrum with seven additional bins down to 0.1 nm [*Solomon et al.*, 2001; *Bailey et al.*, 2002].

The GLOW model provides a full calculation of photoelectron generation and transport based on the *Nagy and Banks* [1970] two-stream algorithm. Since photoelectron flux is initially driven by zenithal solar photoionization, we expect that thermospheric variability will impact its contribution to steady state N_e as previously described for the primary solar photoionization. Herein, we investigate the overall contribution of photoelectron flux to equilibrium mean N_e by running the GLOW model with and without the photoelectron flux algorithm.

GLOW model N_e is compared with ISR-derived mean N_e in Figure 8 for the most highly sampled bin (χ = 45 and $F_{10.7}$ = 155). This figure indicates that photoelectron flux accounts for 50% of the steady state N_e at 110 km, and that the full model agrees with the ISR mean N_e to within ± 10% over the altitude range from 105 to 140 km. A global average of ISR and GLOW model N_e across all parameter space (Figure 9) indicates an agreement to within ±5% for all altitudes between 105 and 180 km.

We now examine the GLOW model, as perturbed with the known thermospheric variability in $T_e(z)$ and T_∞, to see how well estimated var(N_e) agrees with ISR measurements across $F_{10.7} - \chi$ parameter space (Figure 10). In this figure, modeled N_e with appropriate deviation envelopes (purple) are overlain on the ISR variance envelopes (blue) previously shown in Figure 7.

For the ten most highly sampled bins, this figure indicates close agreement of modeled and measured mean N_e, with the exception of a modeled excess for altitudes above approximately 170 km. In general, modeled N_e variance

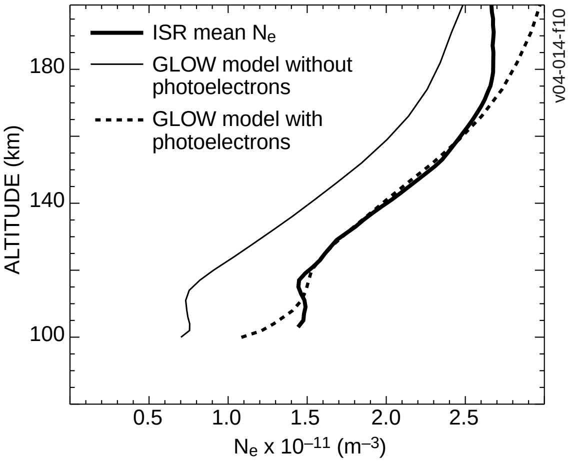

Figure 8. ISR and GLOW Model N_e for $\chi = 45^\circ$ and $F_{10.7}$ = 155.

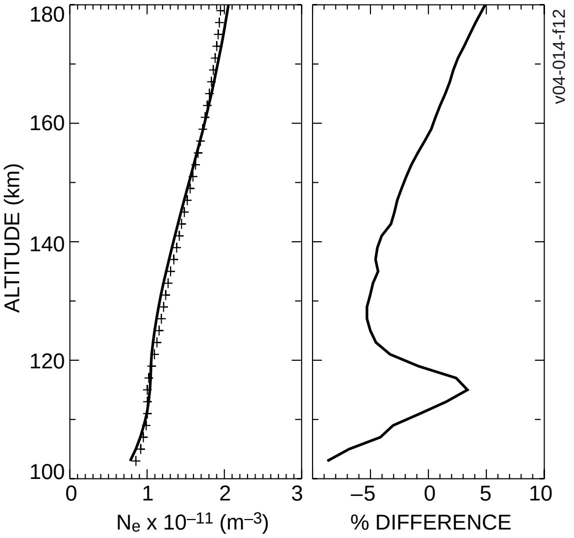

Figure 9. Left hand panel shows ISR mean N_e (crosses) and GLOW model N_e (line) as globally averaged over all bins in $F_{10.7} - \chi$ parameter space. Right hand panel shows ISR – GLOW model deviation.

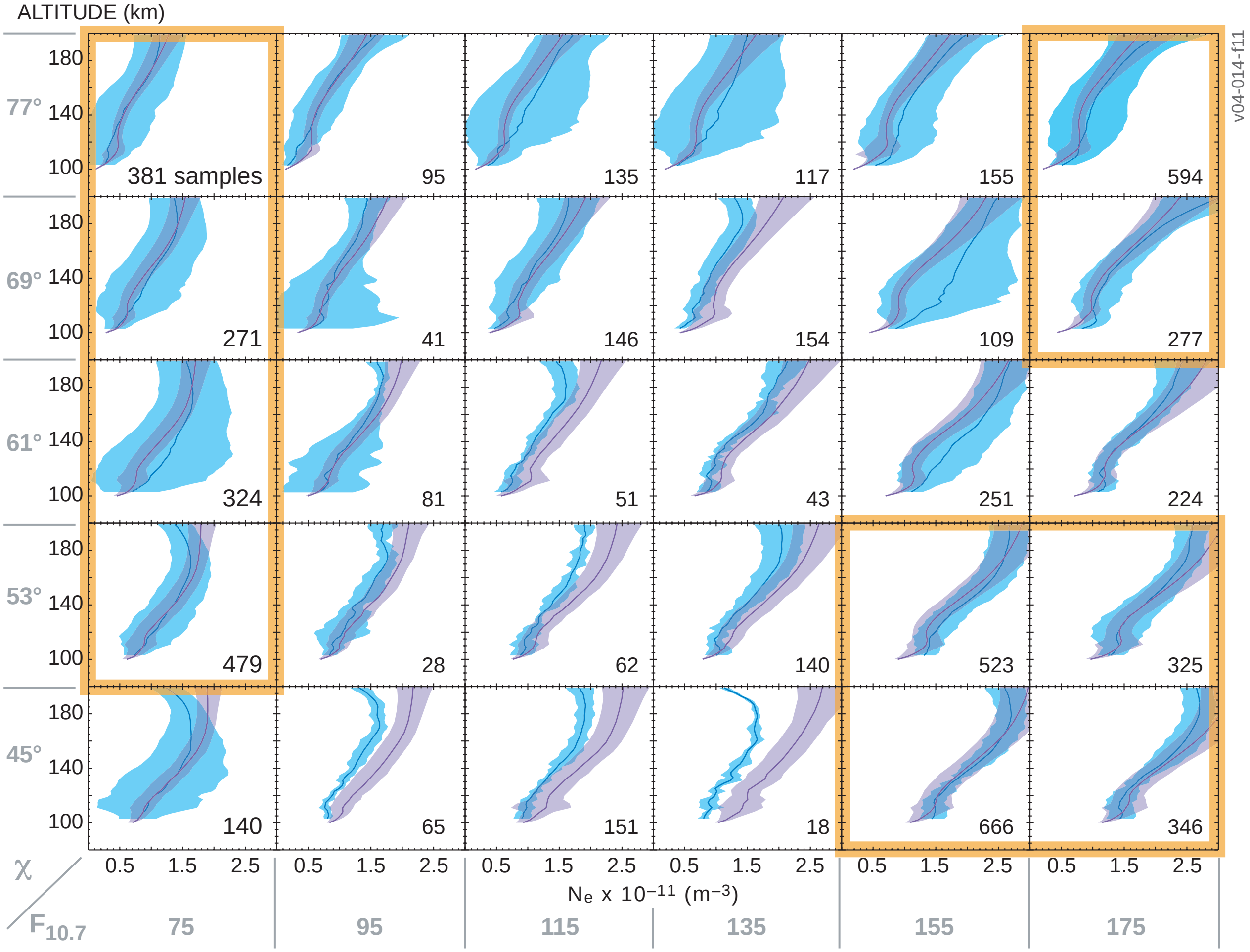

Figure 10. ISR and Modeled Mean and variance N_e.

envelopes are shown to more closely match the ISR measured envelopes at solar maximum. This would imply that the wider variation in N_e measured at solar minimum cannot be reconciled by simply perturbing the thermospheric inputs to the GLOW model. One also notes that the previously identified low-altitude enhancement in ISR mean N_e for solar maximum conditions is at an altitude consistent with the peak altitude for modeled 3 to 7 nm soft X-ray and H Lyman-β ionization [L. Qian, personal communication, 2005]. No such feature is observed for highly sampled solar minimum bins.

5. Discussion

We have assumed herein that our auroral filtering scheme, based on statistics of Σ_H/Σ_P, and including a correction for low-energy diffuse precipitation, is viable. In order to directly test for hard auroral rejection, we compare select $N_e(z)$ bins in Figure 7 with quiet time subauroral $N_e(z)$ profiles acquired at the Millstone Hill Incoherent Scatter Radar corresponding to the same $F_{10.7}$ and χ conditions [*Buonosanto et al.*, 1995]. These Millstone Hill measurements were made with a 40 μs pulse which provides 6 km resolution comparable to the 3 km resolved data reported herein for Sondrestrom. Millstone Hill N_e measurements must be made in winter to match the range of summertime χ measured at the higher latitude Sondrestrom site. These subauroral N_e measurements are presumed to be free of auroral ionization and, in the one case, acquired coincident with sounding rocket EUV spectral measurements. Figure 11 shows that Millstone Hill profiles are within 1 σ of Sondrestrom ISR N_e for altitudes up to 160 km, with the exception of one single data point at 140 km on November 10, 1988.

Figure 11 also shows a significant divergence of Millstone Hill N_e above 160 km relative to the Sondrestrom mean N_e. These enhanced densities, exceeding even those predicted by the GLOW model (Figure 10), occur at an altitude where direct O^+ - molecular ion recombination loss (*E*-region) and O^+ - molecular neutral charge-exchange-recombination loss (*F*-region) are equally dominant, and thus highly sensitive to plasma temperature, neutral temperature, and relative ion - neutral drift. Suppressed ion loss at such altitudes would be expected for the low T_∞ wintertime conditions at the time of the Millstone Hill measurements. However, when we compare mean T_∞ from Sondrestrom ISR $F_{10.7} - \chi$ bins with corresponding Millstone Hill T_∞ for the three dates in question, we see that Millstone Hill is at most 118° K cooler than Sondrestrom — a temperature offset unlikely to have such a dramatic impact on the number density of neutrals available for charge exchange. The discrepancy could also be a lower altitude signature of the *F*-region winter anomaly [*Torr et al.*, 1980] provided that sufficient time has elapsed for downward plasma diffusion from the *F*-layer peak.

Overall, we see good agreement for the three test cases in an altitude range sensitive to energetic electron aurora with $E_0 > 3$ keV. Because these quiet time Millstone Hill N_e profiles are unlikely to be subject to such hard auroral contamination, we conclude that our first stage auroral rejection filter is viable. We now consider our low-energy correction scheme in Section 3.2.

Contamination of daylit profiles by low-energy electron precipitation is unavoidable using our first stage conductance filter and thus a correction is needed. Without such correction, GLOW model predictions are 22 to 36% too low relative to ISR measurements over an altitude range from 100 to 180 km. As we have argued previously, our model for low-energy precipitation is based on the assumption that low-energy auroral contamination is governed by proximity to the instantaneous auroral oval and that for a fixed geomagnetic latitude, this proximity is mostly dependent on MLT. By examining MLT, A_P index, and solar cycle dependence, we show in Figure 6 that low-energy precipitation is mostly dependent on MLT. We now consider the possibility that low-energy auroral contamination impacts our observation of solar cycle dependent N_e variance and low-altitude enhancements.

As pointed out in Figure 7, the ISR measured N_e variance envelope is consistently broader at solar minimum, relative to solar maximum, for highly sampled bins. In order for the observed increase in N_e variability to be attributed to residual low-energy precipitation, we should expect to see significant solar cycle modulation of low-energy N_e. The lower panel of Figure 6 shows little change in mean N_e profile from the $F_{10.7} = 75$ to $F_{10.7} = 175$ bin. We thus conclude that the observed variability in ISR N_e at solar minimum is unlikely to be due to low-energy electron precipitation.

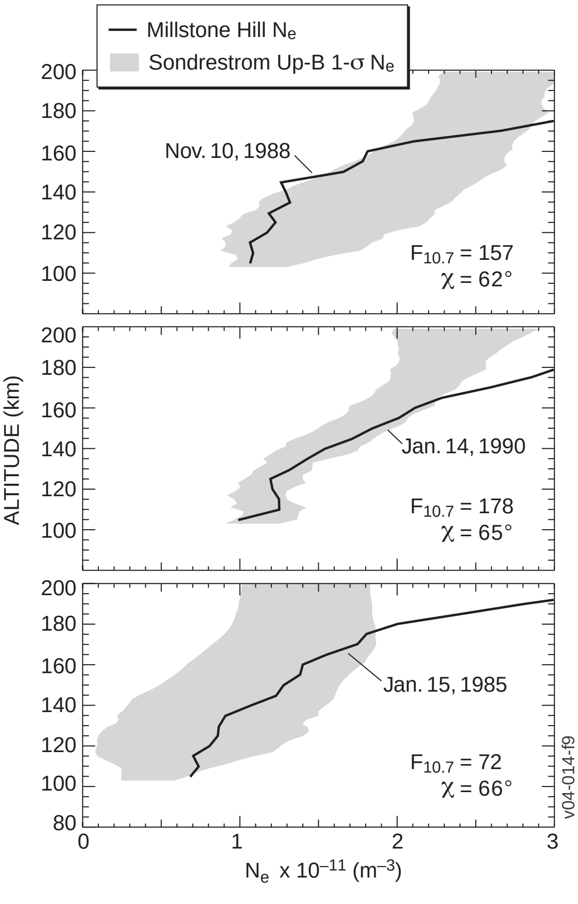

Figure 11. Comparison with Millstone Hill

In these solar minimum bins, ISR measured N_e deviation always exceeds GLOW modeled N_e deviation (due to T_e and T_∞ perturbations) at all altitudes. The variation in N_e given by the GLOW model is based solely on thermospheric perturbation and takes no account for the long-term variability in the EUV solar spectrum. Sondrestrom ISR N_e data, therefore, provides an important signature for solar cycle control of spectral variability.

The low-altitude N_e enhancement noted for 5 out of 6 of the most highly sampled solar maximum bins in Figure 7 is also unlikely to be produced by a low-energy source; soft electron precipitation from 3 keV class electrons will create peak ionization some 15 km higher [*Rees*, 1989]. Proton precipitation would require E_0 on the order of 15 to 20 keV to reach such altitudes [*Galand and Richmond*, 2001], and such energies are excluded by our first-stage conductance filter. As noted previously, this feature occurs at an altitude corresponding to the ionization peak for 3 to 7 nm soft X-

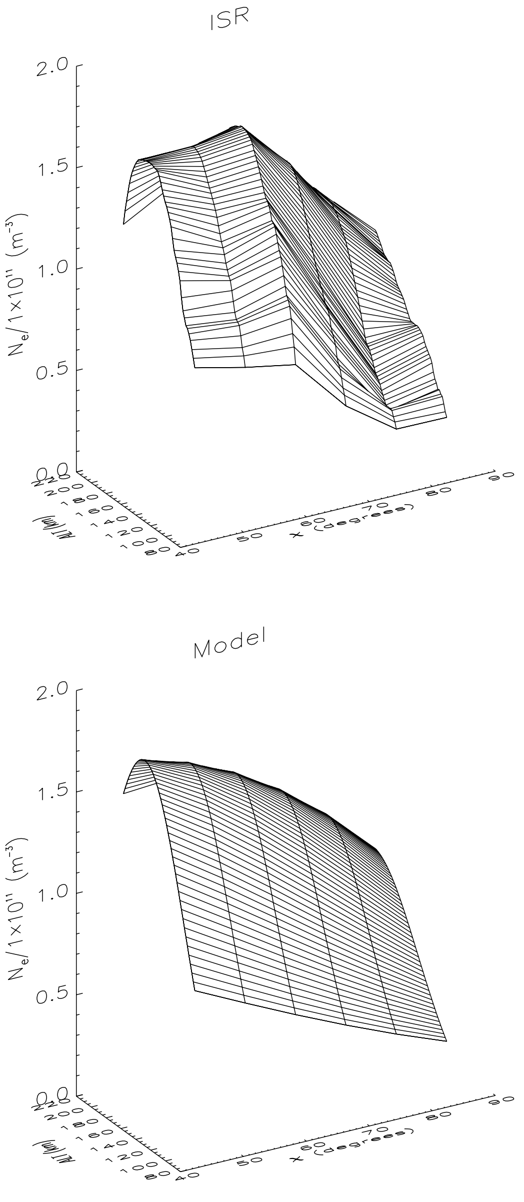

Figure 12. N_e Comparison for $F_{10.7} = 75$

ray and H Lyman-β spectral components. ISR data indicate that this feature is absent for highly sampled solar minimum bins. The GLOW model, which invokes an $F_{10.7}$-dependent modulation of solar spectral flux, reproduces this N_e feature across all bins in $F_{10.7}$ – χ parameter space. Thus, ISR measurements indicate that significant attenuation of soft X-ray and H Lyman-β radiance, below standard GLOW model estimates, is required at solar minimum.

Overall, we see ±5% agreement between GLOW model estimates and ISR mean N_e for altitudes below 170 km. Above 170 km, we note that the GLOW model estimates diverge relative to ISR mean N_e. For solar minimum conditions ($F_{10.7} = 75$) the ISR measured HmF1 is well below 200 km and the GLOW model HmF1 is at or above 200 km (Figure 10, column 1). In column 1, we also note that the ISR measured HmF1 displays a systematic increase with increasing χ — an observation consistent with slant path illumination geometry. The solar maximum column ($F_{10.7} = 175$) suggests this same trend as the topside ISR profiles evolve from asymptotic ($\chi = 45°$) to divergent ($\chi = 77°$). Such systematics are unlikely to result from our A16/LP data merging technique (described in Section 2). A more likely explanation is that the GLOW model is a photochemical equilibrium model unable to account for the vertical ion diffusion that begins to impact plasma density in the *F*1 region. An underestimate in *E*- and *F*-region chemical recombination rates, rates driven primarily by modeled N_2 and O_2 abundance, might also be invoked to explain the GLOW model topside density enhancement. In order to account for such recombination and transport effects on average *F*1 region N_e, an empirical ISR-based model is required.

Ad hoc modifications to the shape of the baseline solar spectra could theoretically be determined by trying to match the altitude profile of ISR mean $N_e(z)$ profiles with the same inversion techniques used to extract primary electron number flux spectra [*Semeter and Kamalabadi*, 2005]. The success of solar spectral inversion will rest on how well ionization contributions from individual λ bins can be partitioned to describe a unique orthogonal basis set. Such analysis is left as a future exercise and we now consider a simple empirical model of photoionization $N_e(z)$. Such a model can provide a better N_e estimate at altitudes above 170 km where GLOW model photochemical equilibrium assumptions break down.

Despite the differences in measured and modeled topside N_e, the GLOW model can assist in the creation of an ISR-based empirical model for NmF1, HmF1, and layer width (W_0) across the $F_{10.7}$ – χ parameter space. Gaussian fits to output from multiple runs of the GLOW model suggest that NmF1 is well represented by a second order function in $F_{10.7}$ and χ, and that HmF1 and W_0 are well represented by first order functions in $F_{10.7}$ and χ. This observation suggests a regularization scheme:

$$\mathrm{NmF1} = A_0 + A_1 x + A_2 y + A_3 x^2 + A_4 y^2 + A_5 xy, \tag{17}$$

$$\mathrm{HmF1} = B_0 + B_1 x + B_2 y, \tag{18}$$

$$\mathrm{W}_0 = C_0 + C_1 x + C_2 y, \tag{19}$$

where x and y are simple indices related to position in $F_{10.7}$ – χ parameter space,

$$x = (\mathrm{F}_{10.7} - 55)/20, \tag{20}$$

$$y = (\chi - 37)/8, \tag{21}$$

and A, B, and C are fit coefficients derived from a least squares estimation approach.

Our first step in deriving A, B, and C is to fit ISR mean $N_e(z)$ with a Gaussian function so as to extract working values for NmF1, HmF1, and W_0 in all 30 $F_{10.7}$ – χ bins. We assume that these working values are estimates for mean NmF1, HmF1, and W_0 with a variance equal to the inverse of the sample number in each bin. As one might expect, arrays of NmF1, HmF1, and W_0 are not smooth across parameter space, especially for transitions from poorly to highly sampled bins. We invoke a least squares regularization scheme that incorporates the functional dependence suggested by equations (17) through (19) above and that is weighted by the number of samples per bin (inverse variance). Table 1 lists numerical values of optimal fit coefficients for this model.

For the previously identified highly sampled bins, our model fits ISR N_e to within 1.5 σ. Figure 12 shows typical ISR model comparison for solar minimum conditions $F_{10.7} = 75$ when the empirical model is well within 1 σ of the ISR mean N_e.

Table 1: Photoionization Model Coefficients

A_0 1.610×10^{11}	A_1 -1.060×10^{10}	A_2 1.405×10^{10}
A_3 5.696×10^{9}	A_4 2.751×10^{9}	A_5 -6.366×10^{9}
B_0 148.5	B_1 6.534	B_2 10.46
C_0 42.52	C_1 5.078	C_2 3.539

6. Conclusions

In this study we have investigated through measurement and modeling the long-term behavior of high-latitude quiet time solar photoionization. Sondrestrom ISR measurements of mean and variance $N_e(z)$ profiles were compiled over a nearly nine-year period on 30 bins defined by $F_{10.7}$ and χ. By comparing high-latitude N_e with mid-latitude measurements at similar $F_{10.7}$ and χ, we have shown that conductance ratio filtering is effective in culling quiet time events from a statistically large database of high-latitude daytime profiles. By characterizing low-energy ionization flux at night as parameterized by MLT, we have been able to remove ionization effects from daytime N_e profiles for electrons with $E_0 < 3$ keV and for protons with $E_0 < 13$ keV.

A major result of our ISR analysis is that N_e variability is greatest at solar minimum and that a persistent low-altitude N_e enhancement is detected only during solar maximum conditions.

In order to further investigate these features, the GLOW model has been invoked. We show that this model, when suitably enhanced for spectral components shortward of 5 nm and with inclusion of photoelectron flux, can predict ISR-based mean N_e to within ±5% across all bins in $F_{10.7}$ – χ parameter space for altitudes up to 170 km. The contribution to steady-state N_e by photoelectron flux is shown to be on the order of 30 to 50% over this altitude range. The failure of GLOW photochemical equilibrium calculations to match ISR measurements of HmF1 in the 170 to 200 km region suggests either the effects of vertical ion transport or chemical recombination and we have introduced an ISR-based empirical model to address this discrepancy.

Thermospheric perturbations to the GLOW model have allowed us to address the source of variability highlighted in the ISR N_e measurements. Specifically, the modeled variance envelope nearly matches the ISR observed variance at solar maximum and accounts for no more than half of the ISR observed variance at solar minimum. We have further shown that low-energy aurora is unlikely to account for such variability due to its relative constancy over the solar cycle. We thus conclude that variability in the solar EUV flux plays a dominant role during solar minimum conditions.

We further note that the altitude associated with the persistent low altitude N_e enhancement is the same as the peak deposition altitude for photoionization due to 3 to 7 nm soft X-ray and H Lyman-β emission. The absence of such an ionospheric enhancement at solar minimum indicates that significant attenuation of soft X-ray and H Lyman-β radiance, below standard GLOW model estimates, is required at solar minimum.

Acknowledgments. We wish to acknowledge the helpful suggestions of Dr. Liying Qian at NCAR. Support for this effort at SRI is provided by the NSF through the Sondrestrom ISR Facility cooperative agreement ATM-0334122. NCAR is supported by the National Science Foundation.

References

Bailey, S. M., C. A. Barth, S. C. Solomon, A modle of Nitric Oxide in the lower thermosphere, *J. Geophys. Res.,* 107, 101029, 2002.

Barrett, J. L. and P. B. Hays, Spatial distribution of energy deposited in nitrogen by electrons, *J. Chem. Phys., 64,* 743, 1976.

Brekke, A. and C. Hall, Auroral ionospheric quiet summer time conductances, *Ann. Geophysicae, 6,* 361, 1988.

Brekke, A., J. R. Doupnik, and P. M. Banks, Incoherent scatter measurements of *E* region conductivities and currents in the auroral zone, *J. Geophys. Res.,* 79, 3773, 1974.

Buonsanto, M. J., P. G. Richards, W. K. Tobiska, S. C. Solomon, Y.-K. Tung, and J. A. Fennelly, Ionospheric electron densities using different EUV flux models and cross sections: Comparison with radar data, *J. Geophys. Res., 100,* 14,569, 1995.

Doe, R. A., J. F. Vickrey, and M. Mendillo, Electrodynamic model for the formation of auroral ionospheric cavities, *J. Geophys. Res.,* 100, 9683, 1995.

Doe, R. A., Kelly, J. D., and E. R. Sanchez, Observations of persistent dayside *F*-region electron temperature enhancements associated with soft magnetosheathlike precipitation, *J. Geophys. Res., 106*, 3615, 2001.

Galand, M., and A. D. Richmond, Ionospheric electrical conductances produced by auroral proton precipitation, *J. Geophys. Res.,* 106, 117, 2001.

Hedin, A. E., MSIS-86 thermospheric model, *J. Geophys. Res., 92*, 4649, 1987.

Hinteregger, H. E., K. Kukuii, and G. R. Gibson, Observational, reference and model data on solar EUV from measurements on AE-E, *Geophys. Res. Lett.,* 8, 1147, 1981.

International Association of Geomagnetism and Aeronomy (Division I Working Group), International geomagnetic reference field: Revision 1985, *J. Geomagn. Geoelectr., 37,* 1157, 1985.

Kelly, J. D., C. J. Heinselman, J. F. Vickrey, and R. R. Vondrak, The Sondrestrom radar and accompanying ground-based instrumentation, *Space Sci. Rev.,* 71, 797, 1995.

Lehtinen, M. S. and I. Häggström, A new modulation principle for incoherent scatter measurements, *Radio Sci., 22,* 625, 1987.

Moen, J. and A. Brekke, The solar flux influence on quiet time conductances in the auroral ionosphere, *Geophys. Res. Lett., 20,* 971, 1993.

Nagy, A. F. and P. M. Banks, Photoelectron fluxes in the ionosphere, *J. Geophys. Res., 75,* 6260, 1970.

Newell, P. T., S. Wing, C.-I. Meng, and Vincent Sigillito, The auroral oval position, structure, and intensity of precipitation from 1984 onward: An automated on-line data base, *J. Geophys. Res., 96,* 5877, 1991.

Newell, P. T., C.-I. Meng, and S. Wing, Relation to solar activity of intense aurorae in sunlight and darkness, *Nature, 393,* 342, 1996.

Rasmussen, C. E., R. W. Schunk, and V. B. Wickwar, A photochemical equilibrium model for ionospheric conductivity, *J. Geophys. Res., 93,* 9831, 1988.

Rees, M. H., *Physics and Chemistry of the Upper Atmosphere*, pp. 39 -43, Cambridge University Press, Cambridge, 1989.

Richards, P. G., J. A. Fennelly, and D. G. Torr, EUVAC: A solar EUV flux model for aeronomic calculations, *J. Geophys. Res., 99,* 8981, 1994.

Rishbeth, H. R. and O. K. Garriott, *Introduction to Ionospheric Physics*, Academic Press, New York and London, 1969.

Robinson, R. M. and R. R. Vondrak, Measurements of E-region ionization and conductivity produced by solar illumination at high latitudes, *J. Geophys. Res.,* 89, 3951, 1984.

Robinson, R. M. and R. R. Vondrak, Characteristics and sources of ionization in the continuous aurora, *Radio Sci.,* 20, 447, 1985.

Robinson, R. M., R. R. Vondrak, K. Miller, T. Dabbs, and D. Hardy, On calculating ionospheric conductances from the flux and energy of precipitating electrons, *J. Geophys. Res., 92,* 2565, 1987.

Schlegel, K., Auroral zone E-region conductivities during solar minimum derived from EISCAT data, *Ann. Geophys., 6,*, 129, 1988.

Semeter, J. L. and R. A. Doe, On the proper interpretation of ionospheric conductance estimated through satellite photometry, *J. Geophys. Res., 106,*, SIA 19-1, 2002.

Semeter, J. L. and F. Kamalabadi, Determination of primary electron spectra from incoherent scatter radar measurements of the auroral *E* region, *Radio Sci.,* in press, 2005.

Solomon, S. C. and L. Qian, Solar EUV energy deposition rate calculations for general circulation models, AGU Fall Meeting, San Francisco, December 2003 (Abstract in *EOS, 84,* F1170, 2003).

Solomon, S. C., P. B. Hays, and V. J. Abreu, The auroral 6300 Åemission: Observations and Modeling, *J. Geophys. Res., 93,* 9867, 1988.

Solomon, S. C. and V. J. Abreu, The 630 nm dayglow, *J. Geophys. Res., 94,* 6817, 1989.

Solomon, S. C., S. M. Bailey, and T. N. Woods, Effect of solar soft X-rays on the lower ionosphere, *Geophys. Res. Lett., 28,* 2149, 2001.

Tobiska, W. K., T. Woods, F. Eparvier, R. Viereck, L. Floyd, D. Bouwer, G. Rottman, and O. R. White, The SOLAR2000 empirical solar irradiance model and forcast tool, *J. Atmos. Sol. Terr. Phys., 62,* 1233, 2000.

Torr, M. R. and D. G. Torr, Recombination of NO^+ in the mid-latitude trough and the polar ionization hole, *J. Geophys. Res., 84,* 4316, 1979.

Torr, D. G., M. R. Torr, and P. G. Richards, Causes of the F region winter anomaly, *Geophys. Res. Lett., 7,* 301, 1980.

Vickrey, J. F., R. R. Vondrak, and S. J. Matthews, Energy deposition by precipitating particles and Joule dissipation in the auroral ionosphere, *J. Geophys. Res., 87,* 5184, 1982.

Walls, F. L., and G. H. Dunn, Measurement of total cross section for electron recombination with NO^+ and O_2^+ using ion storage techniques, *J. Geophys. Res., 79,* 1911, 1974.

Whalen, J. A., A quantitative description of the spatial distribution and dynamics of the energy flux in the continuous aurora, *J. Geophys. Res., 88,* 7155, 1983.

Woods, T. N., F. G. Eparvier, S. M. Bailey, P. C. Chamberlain, J. Lean, G. J. Rottman, S. C. Solomon, W. K. Tobiska, and D. Woodraska, The Solar EUV Experiment (SEE): Mission overview and first results, *J. Geophys. Res.,* in press, 2005.

R. A. Doe, Center for Geospace Studies, SRI International, 333 Ravenswood Ave., Menlo Park, CA 94025. (doe@sri.com)

(Received March 2005; revised May 2005;
accepted June 2005.)